SJER Scientific Journal of Engineering Research

futuristech PT. Teknologi Futuristik Indonesia

Date of publication December 12, 2025, date of current version December 12, 2025.
*e-ISSN: 3109-1725*
*Digital Object Identifier 10.64539/sjer.v2i1.2026.353*

Article

# Mesh Independence and Reynolds Number Sensitivity for External Automotive Aerodynamics Simulations

**Mohammed Almaghrebi[1,2,*], Ahmed Atta Elhussein Ali[3]**

[1] Faculty of Engineering and Information Technology, Al-Saeeda University, Yemen
[2] School of Automotive Engineering, Wuhan University of Technology, 430070, China
[3] School of Business, Sichuan University, China
* Correspondence

The authors received no financial support for the research, authorship and publication of this article.

**Abstract:** Aerodynamic prediction for full scale passenger vehicles relies on the use of mesh resolutions which accurately represent boundary layer evolution and wake dynamics while maintaining reasonable computational expense. To verify the drag prediction for two production-derived vehicle geometries (Notchback and Hatchback) simulated at 15° steady state crosswind using incompressible RANS with SST k–ω turbulence models, the verification process consisted of a systematic set of five progressively refined polyhedral meshes (1.5 million cells - 7.2 million cells) created using a controlled refinement template to maintain consistent near-wall treatment within all five meshes. The drag results showed significant improvement from the coarsest mesh to the finest mesh (≈ 14% improvement for Notchback ≈ 12% improvement for Hatchback) and then clearly exhibited asymptotic results as evidenced by the difference between M4 and M5 decreasing to less than approximately 1.5%, indicating that M4 provides mesh-independent accuracy with over 20% less computational cost than M5. Furthermore, a Reynolds number sweep across the range of representative full-scale Reynolds number values demonstrated that drag is effectively insensitive to Reynolds number once the fully turbulent regime is reached and wake structures between the Notchback and Hatchback. Through this analysis it has been determined that targeted refinement strategies around A-pillar and rear-end separation zones and the near wake will provide the greatest accuracy and cost-effective use of computational resources as compared to uniform global densification, thus providing a validated mesh resolution strategy for using RANS simulations to predict drag for full scale passenger cars under steady state conditions.

**Keywords:** Mesh Independence; Reynolds-Number Sensitivity; Automotive Aerodynamics; Crosswind Flow; $y^+$ Wall Treatment.



## 1. Introduction

Accurate prediction of external automotive aerodynamics requires careful control of mesh resolution near-wall treatment and turbulence modelling, especially for full passenger-vehicle scales where there are thin boundary layers, strong separation zones and 3D wake structures. The large majority of published research comparing grid sensitivity to Reynolds number effects consists of studies on canonical bodies [1]-[3]. Previous work on external aerodynamic CFD and grid sensitivity can be grouped into three categories. First, there are canonical CFD studies and verification studies on grid refinement and discretization-error estimation [4]-[7]. Second, some studies focus on simulations of realistic or generic passenger-car geometries using RANS or hybrid RANS-LES methods, particularly looking at wake resolution and turbulence modelling [8], [9]. Third, research has explored drag-reduction devices and changes in vehicle geometry [6], [10]. Together, these studies offer helpful guidelines but still provide limited combined evidence for full-scale, production derived vehicles in crosswind conditions. The number of research sources that have combined these three aspects into a single study for production-derived full-scale vehicles is notably small. This highlights a clear

gap in verifying mesh independence and Reynolds-number effects for full-scale passenger vehicles under crosswind conditions.

The research literature also tends to focus on a single geometry or on reduced-scale models, thereby providing only limited guidance on the mesh verification process for the analysis of realistic automotive shapes. For typical full-size passenger vehicles with length dimensions between approximately 4 and 4.6 m and velocities between 25 and 35 m/s, the associated Re fall between $\approx 1 \times 10^7$ - $2 \times 10^7$. This high-Re regime can strongly be influenced by mesh distribution when using steady-state simulation with RANS techniques, depending on the type of mesh distribution employed. Specifically, insufficient near-wall and/or wake refinement may lead to distort shear-layer development. Along these same lines, overly fine grids will result in an increase in computational costs without a proportional increase in simulation accuracy when comparing steady-state simulations with RANS techniques [11]-[13]. Consequently, a structured mesh independence assessment must be conducted to ensure that a given computed result reflects the actual physical flow characteristics versus a result representative of discretization [14], [15].

This investigation will utilize the drag coefficient as one principal quantitative comparison and the monotonic convergence of drag coefficients in steady external flow as the primary means of establishing confidence in the mesh's ability to accurately represent the physical flow characteristics. The lift and side-force components will also be compared to confirm that the qualitative trend in lift and side-force components is consistent across the entire set of meshes. In addition, analysing the sensitivity to Re provides further verification of whether the flow has reached the asymptotic fully turbulent regime in which the aerodynamic coefficients become effectively Re-independent. Although the concept of Reynolds number independence is well established in the literature, few studies have reported, for production-derived vehicle geometries, the specific ranges of Re corresponding to the stabilization of aerodynamic coefficient values.

Clarifying this behavior is particularly relevant for steady RANS simulations that target operational conditions between $Re \approx 1.1 \times 10^7$ and $Re \approx 1.9 \times 10^7$. To address these gaps, the present study evaluates mesh-convergence and Reynolds-number sensitivity for two full-scale passenger-vehicle geometries a Notchback and a Hatchback representing two widely used rear-end typologies with distinct separation characteristics. Using identical numerical settings, including wall-modeled SST $k-\omega$ turbulence, a target spacing of $30 \leq y+ \leq 100$, and five systematically refined polyhedral meshes (1.5–7.2 million cells), the analysis examines whether consistent verification trends are maintained across both geometries. Mesh independence is quantified through the relative variation in drag between successive grids, while Re sensitivity is assessed across the ranges $Re = 1.33 \times 10^7 - 1.89 \times 10^7$ (Notchback) and $Re = 1.16 \times 10^7 - 1.64 \times 10^7$ (Hatchback). The objective of this work is to establish a mesh resolution that yields numerically stable aerodynamic predictions with minimal sensitivity to grid density and Re. The findings offer practical guidance relevant to steady RANS–SST simulations of full-scale passenger vehicles with comparable geometric and aerodynamic characteristics. The focus of the present study is verification, full experimental validation lies outside the scope of this mini-paper.

The current study is different from earlier research in three main ways. First, while much of the existing literature focuses on canonical bluff bodies or reduced-scale car models, we look at two full-size production vehicles with different rear-end designs under the identical crosswind conditions. Second, we create the mesh hierarchy using a single polyhedral refinement template. This ensures consistent wall-modelled $y^+$ values and mesh quality across all levels. As a result, we can clearly assess how grid density impacts drag prediction. Third, by combining mesh-independence verification and Reynolds-number sensitivity analysis within the same RANS-SST framework, the study offers a practical verification strategy. This method can be directly used in steady external-aerodynamics simulations for similar passenger vehicle designs.

The remainder of this paper first outlines the numerical methodology and governing equations used in the simulations, then presents and discusses the results of the mesh-independence and Reynolds-number sensitivity analyses, including mesh quality and computational cost, and finally summarizes the main conclusions and suggests directions for future work.

## 2. Methodology

The methodology adopted in this work is designed to verify mesh independence and Reynolds-number sensitivity for steady external automotive aerodynamics under an oblique-flow condition. The main steps of the numerical workflow are summarized in Figure 1. The study follows a simple sequence. First the full-scale notchback and hatchback geometries are rebuilt from manufacturer blueprints and the computational domain with a 15° crosswind inflow is defined. Next a family of five polyhedral meshes M1–M5 with controlled near wall resolution is generated and steady incompressible RANS SST k–ω simulations are run on each mesh to check mesh independence. Convergence is checked by monitoring residuals and the stabilization of drag, lift and side force, and mesh independence is then assessed by comparing the change in drag between successive mesh levels and selecting a cost-effective mesh that is close to the finest grid. Finally, a Reynolds number sweep is performed on the selected mesh by varying only

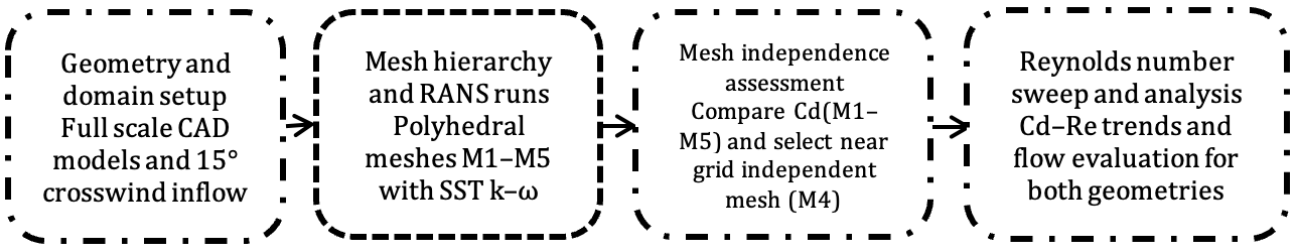


**Figure 1.** Flowchart of the numerical workflow from geometry and domain setup to mesh generation RANS simulations and Reynolds number sensitivity analysis.

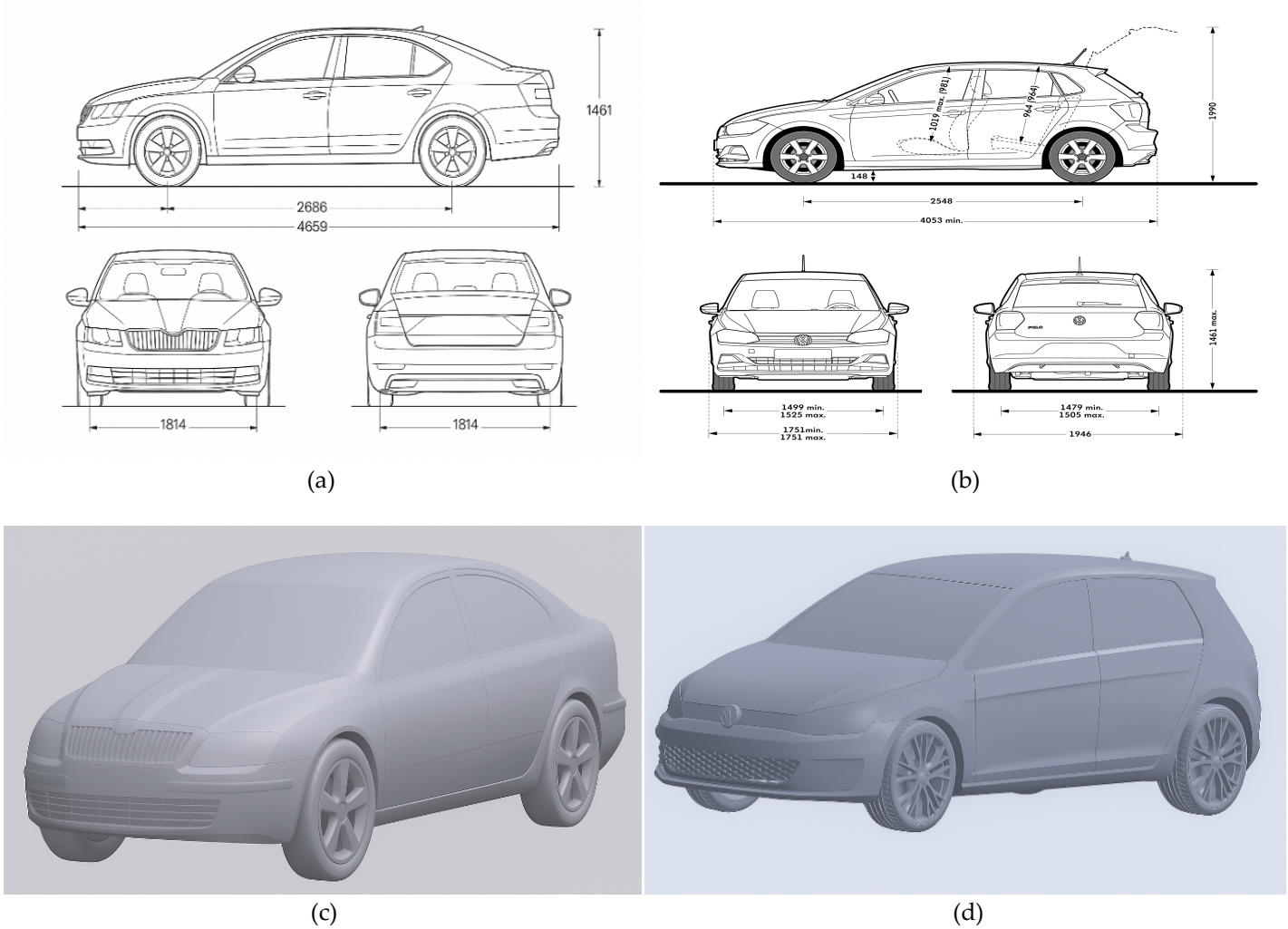


**Figure 2.** Manufacturer blueprints and simplified CFD 3D models of the two vehicles: (a) Notchback (Škoda Octavia) – blueprints; (b) Hatchback (Volkswagen Polo) – blueprints; (c) Notchback– simplified CFD model; (d) Hatchback – simplified CFD model.

the inlet velocity, and the resulting changes in drag are analyzed to identify the range where the coefficients become effectively Re independent for both vehicle geometries.

### 2.1. Vehicle Geometries and Reconstruction

Two types of full-sized geometries for passenger vehicles were analyzed: a Notchback (Škoda Octavia) and a Hatchback (Volkswagen Polo). Manufacturer-supplied technical drawings were reconstructed in SolidWorks 2020 during these studies following the same methodologies for performing surface-cleaning procedures and generating solids as used before for other CFD studies based on manufactured models [16]-[19].

The full-scale geometries retained the predominant geometric attributes, thus, various fine-scale details, including mirrors and handles, were not used in this study to simplify the full-scale geometry while retaining the flow attributes. The results of previous studies [20] indicate that very minor geometrical details do not have nearly the same significant effect on the global aerodynamic coefficients as do the rear-geometry and underbody topology.

Thus, all relevant primary length scales (i.e., overall length, width, height, and rear overhang) were retained in the reconstructed CAD models required to represent realistic development of the boundary layer separation zones, and the wake structures required to accurately resolve

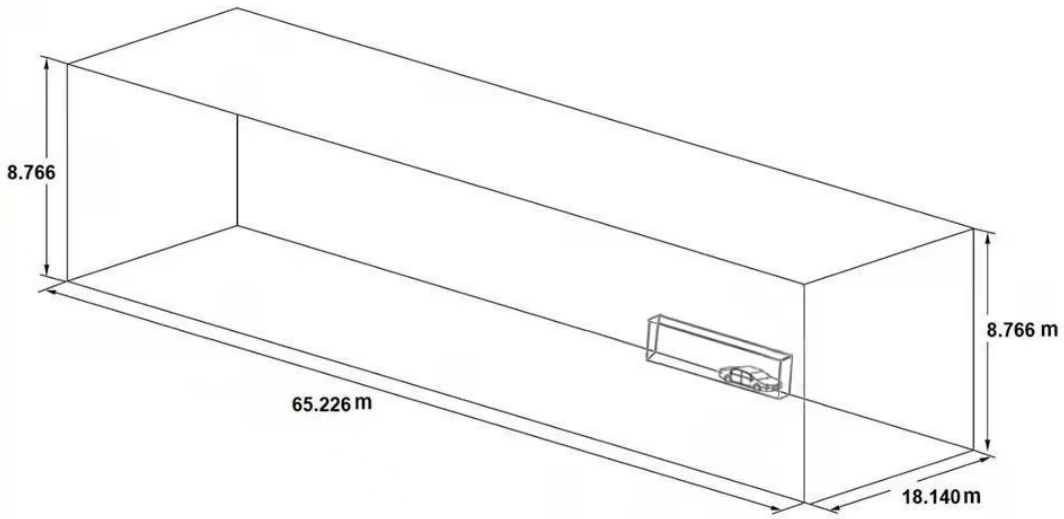


**Figure 3.** Schematic of the computational domain and vehicle placement used for the external aerodynamics simulations.

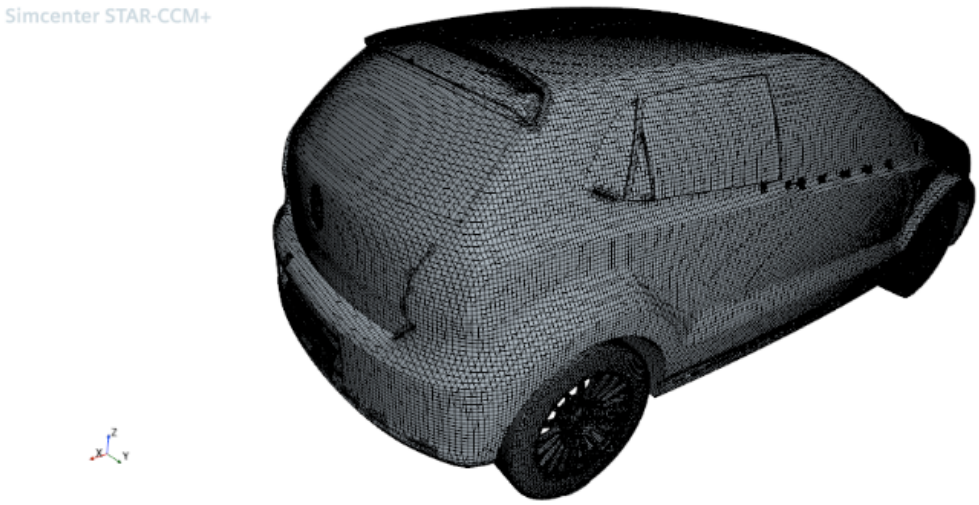


**Figure 4.** Surface-Based Refinement Template.

**Table 1.** Summary of the flow conditions used in the study.

| Quantity | Symbol | Value |
|---|---|---|
| Reference velocity | $U_x$ | 34.8 m/s |
| Streamwise component | $U_x$ | 33.6 m/s |
| Lateral component | $Uy$ | 9.0 m/s |
| Yaw angle | $\beta$ | 15° |
| Turbulence intensity | $TI$ | 1% |
| Turbulence length scale | $Lt$ | (0.05H) |
| Air density | ϱ | 1.204 kg/m³ |
| Dynamic viscosity | $\mu$ | $1.825\times10^{-5}\ Pa\cdot s$ |
| Reynolds range (Hatchback) | $(Re)$ | $1.16\times10^{7}$ - $1.64\times10^{7}$ |
| Reynolds range (Notchback) | $(Re)$ | $1.33\times10^{7}$ - $1.89\times10^{7}$ |

with the mesh resolution and were therefore included in the final generated geometries. The blueprint-derived dimensions are illustrated in Figure 2 together with the simplified CFD-ready geometries of the Notchback and Hatchback vehicles.

The two different rear-end designs were chosen to represent distinct separation behaviors of the two designs. The two vehicle body styles were selected because their rear-end geometries represent distinct flow-separation behaviors: the notchback exhibits a gently sloped trunk, while the hatchback features a more abruptly truncated tail. Each design was a common vehicle style used to observe the process of predicting vehicle without focusing on detailed aerodynamic performance comparisons between these two body configurations.

## 2.2. Computational Domain and Inflow Conditions

The wind-tunnel-type enclosure serves as the computational domain and is built according to recommended guidelines for full-scale automotive CFD by extending 6.5 vehicle lengths upstream, 10 lengths downstream, and 4

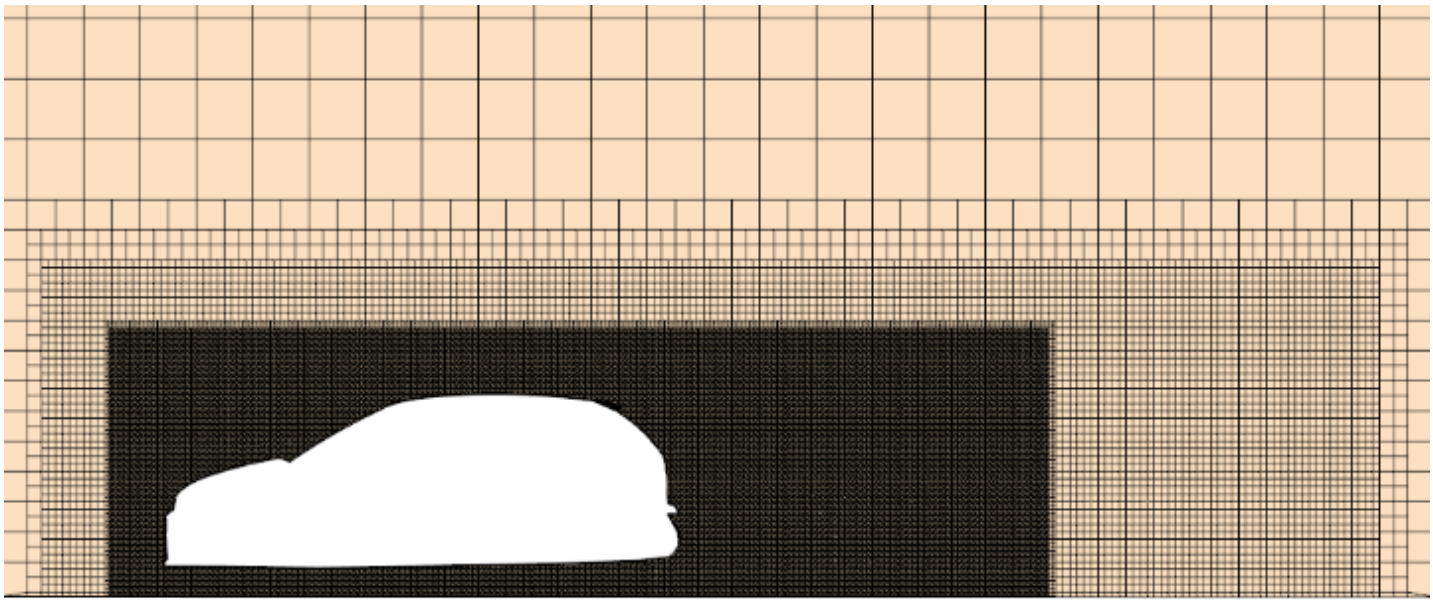

**Figure 5.** Polyhedral Surface and Volume Mesh.

widths in both lateral and vertical directions [21]-[24]. The computational domain layout and boundary configuration are displayed in Figure 3. The baseline for both the mesh independence and the Reynolds sensitivity analysis are based on a single oblique flow condition.

The fixed yaw angle of 15 degrees defines the free-stream direction, and from the reference speed of 34.8 m/s, the inlet velocity components were derived. The ground plane is modeled as a moving wall, while all of the surfaces of the vehicle are modeled as a no-slip walls. The lateral and upper boundaries are modeled as slip walls, with zero normal velocity and zero shear. The turbulence quantities needed for the SST k-ω model have been established under a low-intensity open road condition with the prescribed turbulence intensity and length scale. The turbulence and fluid properties at the inlet are summarized in Table 1.

## 2.3. Mesh Generation

Using ANSA, the computational mesh was created according to an approach, called a structured refinement strategy, for evaluating mesh convergence at all levels of grid spacing by maintaining near wall resolution within all levels of the grid uniformly [25]. Five refined volume meshes (M1 thru M5) were developed by taking the same refinement template and uniformly reducing the target cell size by an equal amount on all 5 meshes. The surface discretization for the examination was performed with curvature controlled triangular elements, using a maximum surface size of 2-4 mm for the front fascia and window regions, 4-8 mm for the wheelhouses, and 8-12 mm for the other body surfaces. The total number of surfaces meshes that were included in this mesh was greater than 150,000. In all mesh levels, this level of resolution was maintained to effectively isolate the effects of refinements made to volume cells. Figure 4 illustrates the structured refinement blocks used in the procedure for controlling mesh density. All refinement levels, and thus geometry, are taken from the same refinement template. This ensures that all differences found in aerodynamic forces result solely from differences in grid density and not by a change in mesh topology. A total of 10 prism layers were used to generate stable near-wall resolution within a recommended range of $30 \leq y^{+} \leq 100$ (some variation less than ±5%). Beyond the prism layers, the remaining volume was populated with isotropic polyhedral cells. Figure 5 provides a depiction of the polyhedral mesh topology around the vehicle and illustrates the smooth transition between refinement zones and the absence of large discontinuities in aspect ratio. This indicates that the mesh can clearly resolve geometric curvature (e.g., wheelhouse, A-pillar, roof/rear junction) with minimal or no distortion or cell skewness.

All five mesh levels achieved the required standard quality metrics for external automotive aerodynamics: skewness < 0.6 and non-orthogonality < 45°. Overall, the five meshes, having 1.5 to 7.2 million cells each, represent a consistent and geometrically controlled path to refinement.

## 2.4. Solver Settings

The simulations were executed using a steady incompressible RANS solution algorithm employing the SST k-ω turbulence model, which is well established robustness in predicting separated flows under yawed conditions with external flow fields [26]-[28]. Although crosswind flows are inherently unsteady, the steady RANS modelling approach is typically accepted within industry for the calculation of time-averaged aerodynamic loads [29], which is the primary focus of this validation study. Transport equations were discretized using second-order upwind schemes for momentum, turbulent kinetic energy and specific dissipation rate, with second order interpola-

tion of pressure and reconstruction of gradients by least squares methods.

The solver used a fully implicit coupled algorithm with multigrid acceleration with adaptive under-relaxation controls added for speed of convergence, these controls only impact the iterative solution path but do not affect the ultimate solution result. Convergence was measured by two complementary indicators: residual error for all governing equations consistently decreased to around $10^{-3}$, and drag coefficient stabilized and remained within approximately 1% of its mean value over the last few iterations, therefore representing a dependable measure of the steady state value of each independent case over all levels of mesh refinement.

All boundary conditions, inlet turbulence quantities, fluid properties, and numerical parameters were held constant between each of each Reynolds-number realization so as to allow for direct comparison of results. The mesh hierarchy was also checked for oscillatory behavior or non-monotonic convergence and it was found that aerodynamic force estimates reached their asymptotic values smoothly with refinement of mesh.

### 2.5. Verification Workflow

The verification procedure is based on a controlled, systematic approach that isolates the effects of mesh refinement (grid size) and Reynolds number (Re) by keeping all other parameters fixed [30], [31]. mesh resolution for each of the meshes (M1 to M5) used the identical method of generating a mesh, the computational solver was set-up with identical settings for all five meshes, the boundary condition set up, initialization of turbulence, and associated near-wall treatments were the same for each case. Thus, any deviation in predicted aerodynamic forces is attributable to either the differences in the density of the grid or the Re at the freestream location of the grid. The results were considered representative of the steady-state solution for the entire mesh hierarchy. The residuals from the governing equations dropped to a level of approximately $10^{-3}$, and the drag coefficient was shown to stabilize within about 1% and did not change more than 1% across the iterations leading up to steady-state, thereby providing a consistent quantitative standard to determine the attainment of steady-state for the entire mesh hierarchy.

In order to assess grid independence, the rate of change in drag between each successive mesh grid (M1 to M5) was compared and interpreted relative to the anticipated solution based on a monotonic approach toward an asymptotic value. Each of the meshes was verified explicitly for the absence of oscillatory and/or non-monotonic trends normally associated with inadequate refinement in separation flow fields. Using the converged steady-state solution for each mesh grid that had been previously verified, the sensitivity of Reynolds number was evaluated by progressively increasing the reference speed at the inlet, all parameters in the geometric, numerical and turbulence model were kept constant throughout the sensitivity evaluation period.

The above methodology guarantees that all changes in the aerodynamic coefficients are representative of actual true Re-effects, any deviation from Re affects all aerodynamic coefficients, not only the drag coefficient. Additional components of aerodynamic forces (lift component and side-force component) were monitored throughout the verification process to confirm that no unusual variation occurred with respect to, for example, lift and side force stability during the time it took to determine drag stability. The combined use of the above methodology establishes a solid, reproducible and methodologically consistent basis to interpret the mesh independence and Re independence trends found in the results section of the report.

### 2.6. Computational Resources

All simulations were executed on a Linux-based high-performance workstation equipped with dual Intel Xeon processors and 32 parallel compute cores. This core count was selected to maintain high parallel efficiency and avoid the communication overhead typically observed when exceeding 32–48 cores in polyhedral RANS calculations. The system provided 128 GB of RAM and operated under a CentOS/RHEL environment. Simcenter STAR-CCM+ (academic license) handled the computations using its MPI-based parallel framework, ensuring consistent runtime scaling across mesh levels M1–M5.

## 3. Governing Equations

The airflow around the vehicle is modeled as an incompressible, isothermal, Newtonian fluid governed by the steady Reynolds-Averaged Navier–Stokes (RANS) equations. This formulation, extensively used in CFD simulations [32] and in automotive aerodynamic studies [16]-[18] , results from applying Reynolds decomposition to the instantaneous velocity field, which introduces turbulent stresses requiring closure through a turbulence model.

### 3.1. Continuity and Momentum Equations

The conservation of mass is enforced through the continuity Equation 1, which ensures that the mean velocity field remains divergence-free and no artificial sources or sinks of mass are introduced:

$$\nabla \cdot \mathrm{U} = 0 \tag{1}$$

where  is the mean velocity vector.

The mean momentum balance is expressed by the steady RANS equation:

$$\rho(\mathbf{U} \cdot \nabla)\mathbf{U} = -\nabla p + \nabla \cdot [\mu(\nabla \mathbf{U} + \nabla \mathbf{U}^T) - \rho \mathbf{u}'\mathbf{u}'] \tag{2}$$

which is widely used in CFD applications [33] and is commonly adopted in road-vehicle simulations for predicting aerodynamic forces [16]-[18], [34].

Here, u′u′ denotes the Reynolds stress tensor, representing momentum transport by turbulent fluctuations. Equation 2 governs the pressure and shear fields that determine drag and lift.

### 3.2. Boussinesq Approximation

To relate the turbulent stresses in Equation 2 to mean flow gradients, the Boussinesq hypothesis (3) is applied:

$$-\rho \mathbf{u}'\mathbf{u}' = 2\mu_t \mathbf{S} - \frac{\mathbf{2}}{\mathbf{3}}\rho k \mathbf{I}, \tag{3}$$

where $S$ is the strain-rate tensor, $k$ the turbulent kinetic energy, and $\mu_t$ the eddy viscosity. This approximation provides a link between the turbulent stresses and local velocity gradients and is routinely applied in automotive external-flow simulations [34].

### 3.3. SST k–ω Turbulence Model

To determine the eddy viscosity, the Shear-Stress Transport (SST) $k-\omega$ model is used, originally formulated by [11] and widely validated for separated vehicle wakes and adverse pressure-gradient flows.

The transport equation for turbulent kinetic energy is:

$$\mathbf{U}\cdot\nabla k = P_k - \beta^* k\omega + \nabla\cdot[(\mu+\sigma_k\mu_t)\nabla k], \tag{4}$$

while the specific dissipation rate evolves according to:

$$\mathbf{U}\cdot\nabla\omega = \alpha\frac{\omega}{k}P_k - \beta\omega^2 + \nabla\cdot[(\mu+\sigma_\omega\mu_t)\nabla\omega] + 2(1-F_1)\sigma_{\omega 2}\frac{1}{\omega}\nabla k\cdot\nabla\omega. \tag{5}$$

The eddy viscosity is then computed by:

$$\mu_t = \rho\frac{k}{\omega}f_{\mathrm{SST}}, \tag{6}$$

where $f_{\mathrm{SST}}$ limits excessive shear stress.

Equation 4 – 6 determine separation onset and wake structure, core contributors to drag sensitivity with mesh resolution.

### 3.4. Near-Wall Treatment and the Role of $y^+$

Given the high Reynolds numbers of road vehicles ($Re$ ~ $10^7$), fully wall-resolved LES is impractical, hence, wall-modeled RANS is employed following standard guidelines.

The dimensionless wall distance is defined as:

$$y^+ = \frac{\rho u_\tau y}{\mu}, \tag{7}$$

where $y$ is the distance of the first cell, $\tau w$ the wall shear stress, and $(u\tau = \tau w/\rho)^{0.5}$ the friction velocity.

To ensure accurate wall-function behavior and turbulence production, the mesh must satisfy the recommended range:

$$30 \le y^+ \le 100. \tag{8}$$

The $y^+$ maps shown later confirm that the prism-layer design in this study adheres to this requirement.

### 3.5. Mesh- and Reynolds-Sensitivity Metrics

Mesh convergence is assessed using the drag coefficient:

$$C_d = \frac{D}{\frac{1}{2}\rho U_\infty^2 A}, \tag{9}$$

which exhibits smooth convergence behavior for automotive bluff bodies.

Relative changes are computed using:

$$\Delta C_d^{(i)} = \left|\frac{C_d^{(i+1)} - C_d^{(i)}}{C_d^{(i)}}\right| \times 100\%. \tag{10}$$

Re is defined as:

$$Re = \frac{\rho U_\infty L}{\mu}, \tag{11}$$

where $L$ is the characteristic vehicle length.

For sufficiently high $Re$, global coefficients approach an asymptotic regime in which they become effectively independent of Re.

Near-wall shear behavior may also be characterized by the skin-friction coefficient:

$$C_f = 2\left(\frac{u_\tau}{U_\infty}\right)^2, \tag{12}$$

linking mesh-dependent wall-stress accuracy to global drag prediction.

Finally, the discretization uncertainty can be estimated using the Grid Convergence Index (GCI):

$$GCI = F_s\frac{|\emptyset_2 - \emptyset_1|}{\emptyset_1(r^p - 1)} \times 100\%, \tag{13}$$

supporting the mesh-independence interpretation drawn from Equation 10.

## 4. Results

### 4.1. Mesh Independence Study

Table 2 summarizes the Cd across the five mesh levels (M1 - M5) for both the Notchback and Hatchback configu-

**Table 2.** Mesh Characteristics and Drag Coefficient for Notchback and Hatchback Configurations.

| Mesh | Growth rate in Euler region | Growth rate in RANS region | Approx. filter size in DES region | Total number of cells (millions) | Notchback | | Hatchback | |
|---|---|---|---|---|---|---|---|---|
| | | | | | Drag Coefficient (Cd) | % Change in Cd | Drag Coefficient (Cd) | % Change in Cd |
| M1 | 1.3 | 1.2 | N/A | 1.5 | 0.333 | -- | 0.391 | -- |
| M2 | 1.2 | 1.2 | N/A | 3.6 | 0.315 | 5.4% | 0.370 | 5.3% |
| M3 | 1.15 | 1.2 | N/A | 4.5 | 0.298 | 5.1% | 0.355 | 4.1% |
| M4 | 1.1 | 1.2 | 100 mm | 6.0 | 0.289 | 3.0% | 0.347 | 2.3% |
| M5 | 1.1 | 1.2 | 50 mm | 7.2 | 0.285 | 1.4% | 0.343 | 1.2% |

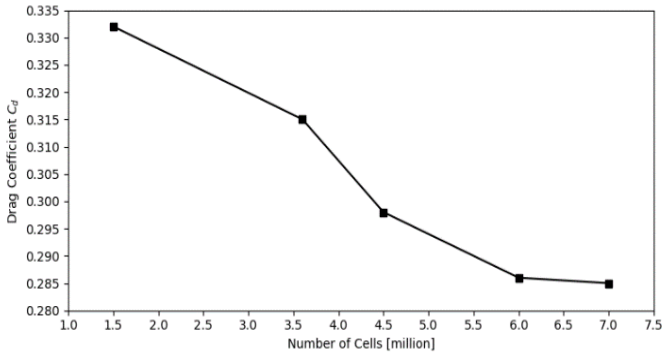


(a) Notchback

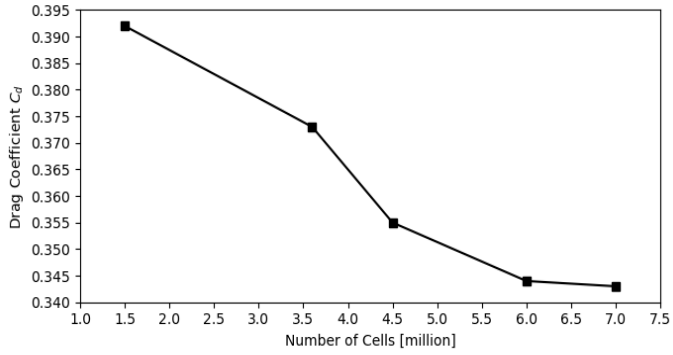


(b) Hatchback

**Figure 6.** Variation of the drag coefficient (Cd) with the number of mesh cells for the two vehicle configurations using the SST k–ω turbulence model: (a) Notchback; (b) Hatchback.

rations. Cd is defined as the total aerodynamic force integrated over the respective surface area and making it an appropriate indicator a primary means of assessing mesh-induced variations in bluff body flows. On both geometries, as the mesh resolution is increased, the Cd values decrease consistently and monotonically, this is indicative of an improved resolution of the regions of separation and the rear wake. Furthermore, the values decrease steadily and consistently as the mesh is refined, this indicates an improved representation of separation lines, near-wake structures and pressure gradients. The trend is documented in Figure 6, which presents a plot of Cd versus the total number of cells for both vehicle geometries. The respective curves show rapid changes between coarse meshes M1-M3, followed by clear asymptotic flattening between M4 and M5, confirming that the solution is approaching a grid-independent solution. In the case of the Notchback, the Cd decreases from 0.333 at the coarsest grid (M1) to 0.285 at the finest grid (M5), which represents an overall reduction of approximately 14%. The same pattern is apparent for the Hatchback, where the Cd decreases from 0.391 (M1) to 0.343 (M5). Of particular significance is that the relative difference between the successively coarser and finer meshes, as measured using Equation 10, becomes progressively smaller for both geometries.

The Notchback has reductions of 5.4%, 5.1%, 3.0% and 1.4% from M1 → M2 → M3 → M4 → M5, the Hatchback has reductions of 5.3%, 4.1%, 2.3% and 1.2% over the same hierarchy of meshes. The consistent reduction of Cd across both vehicle shapes indicates that the refinement strategy has successfully achieved a steady, smooth approach to an asymptotic, solution with no indicators of reverse or stagnation, which would suggest that inadequate or uneven refinement has occurred in the mesh hierarchy. Based on the trends noted, the mesh level M4 represents a mesh-independent solution accurate within approximately 1-2% of the finest grid M5 with substantially less computational effort.

For both vehicle geometries, the absolute change in Cd between the meshes M4 and M5 is very small (0.004 for the Notchback and 0.004 for the Hatchback), which is within the acceptable error limit used in typical automotive CFD verification studies [22]. The similarity in convergence behavior of two vehicles with different rear-end geometries further strengthens the robustness or reinforces the robustness of the refinement hierarchy and indicates that the selected mesh refinement strategy is effective at resolving the essential flow features that contribute to drag generation.

The drag levels obtained from the mesh-independence analysis are also compared with external references to check their plausibility. For the notchback configuration, the finest-grid value Cd = 0.285 differs by less than 1% from the manufacturer-reported value Cd ≈ 0.288 for the corresponding production vehicle, and it falls within the range reported for notchback-type geometries in previous aerodynamic and CFD studies [2], [4]-[6]. For the hatchback configuration, the present value Cd = 0.343 is moderately higher than the nominal catalogue value Cd ≈

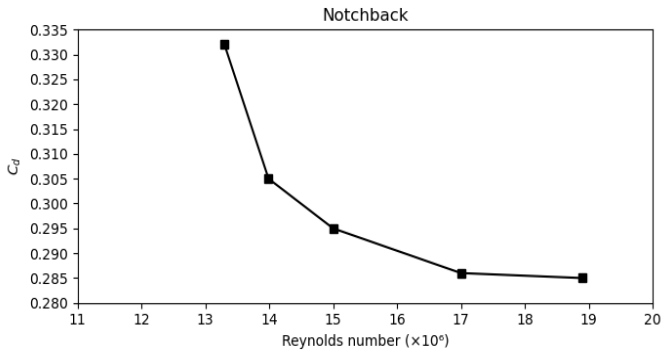


(a) Notchback

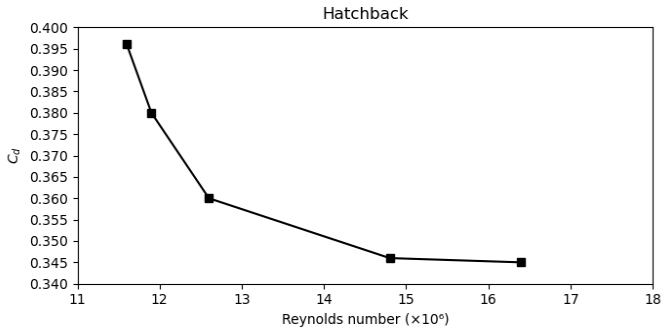


(b) Hatchback

**Figure 7.** Variation of drag coefficient (Cd) with Reynolds number for the two vehicle configurations: (a) Notchback; (b) Hatchback.

0.32 quoted for Volkswagen Polo variants [4] ,[7], [8]. This difference is expected, since the current simulations are performed at a 15° crosswind angle with a simplified geometry and stationary wheels, whereas published catalogue values and several CFD studies usually consider straight-ahead flow and more detailed front-end modelling [9]. In addition, previous work has shown that changes in front-end components, ride height and tire deformation can modify the drag of road vehicles by a few per cent [4], [5], which is comparable to the differences observed here between the present CFD results and catalogue data. Overall, the Cd levels and their monotonic, asymptotic convergence with mesh refinement in this study are consistent with RANS-based CFD and combined CFD/experimental investigations of notchback and hatchback vehicles reported in the literature [4].

### 4.2. Reynolds Number Sensitivity

Reynolds number's impact on the drag coefficients was studied through a series of tests, by changing only the reference velocities (and keeping a constant yaw angle of 15°) and charting the relationship between the drag coefficient (Cd) and Reynolds number for both hatchback and notchback vehicles in Figure 7. Both vehicles followed the same trend, as Reynolds number increases, drag coefficients fall rapidly at lower Reynolds numbers (due to the transition happening much sooner and a thinner boundary layer) then enter into an asymptotic curve where they continue to level off toward a fully turbulent flow at higher Re. In both cases studied, the rate of decrease of Cd as Re increased was significantly slower for Re > approximately $1.7 \times 10^7$ in comparison to Cd for lower Reynolds numbers, illustrating the transition from a viscous-dominated to an inertial-dominated flow. The hatchbacks exhibit a similar decreasing trend as Re increases (between measurements of 1.16 to 1.64 × $10^7$) in Cd, corresponding with the hatchback shows a similar trend to the notchback. Both hatchbacks and notchbacks also demonstrate a consistent flattening of the curve, indicating that both vehicles have entered a Reynolds-independent regime at the highest Re numbers. In addition to confirming that Re numbers tested are all operating under the asymptotic aerodynamic regime associated with full-scale highway speeds of automobiles confirming mesh-independence as outlined in Section 4.1.

### 4.3. Mesh Quality Assessment

Quantitative assessments of the mesh quality for M4 (the chosen mesh level) were performed for each of the two different vehicle configurations to verify that sufficient numerical resolution was achieved in each of the mesh-independence and Reynolds-sensitivity studies. The skewness for both the Hatchback and Notchback models is approximately 0.7 (average) with the maximum values approaching 0.8 consequently, both the mean and maximum skewness values are below the commonly accepted upper limits of polyhedral meshes used for external automotive aerodynamics, thus not producing the irregularities due to gradient reconstruction or spurious diffusion effects normally associated with skewness values close to 0.85. In addition, the similarity of the skewness values for the two vehicle geometries implies that the Mesh did not create any geometry-specific distortions that would implement a bias into the drag predictions.

The corresponding wall-$y^+$ distributions for both vehicle configurations at mesh level M4 are shown in Figure 8. The non-orthogonality remained within stable numerical limits with the maximum angles around 45° which are within the allowable limits of second-order finite-volume approximations and, importantly, are particularly strong in regions of the models with sharp curvature or flow turning, for example, around the A-Pillar, Wheel Arch transition regions and trailing edges of the roof and rear window. The fact that no solver divergence or correction-loop inflation was experienced supports the fact that the Mesh did not create pathological angles which are typically detrimental to RANS-robustness. As expected for a wall-modeled RANS solution, the prism-layer topology was Anisotropic with the aspect ratio sat the near-wall layers approaching ≈120, while the aspect ratios in the outer flow were closer to ≈15. The distribution of the aspect ratios matches the requirements for properly resolving the boundary-layer velocity gradients with minimal normal refinement.

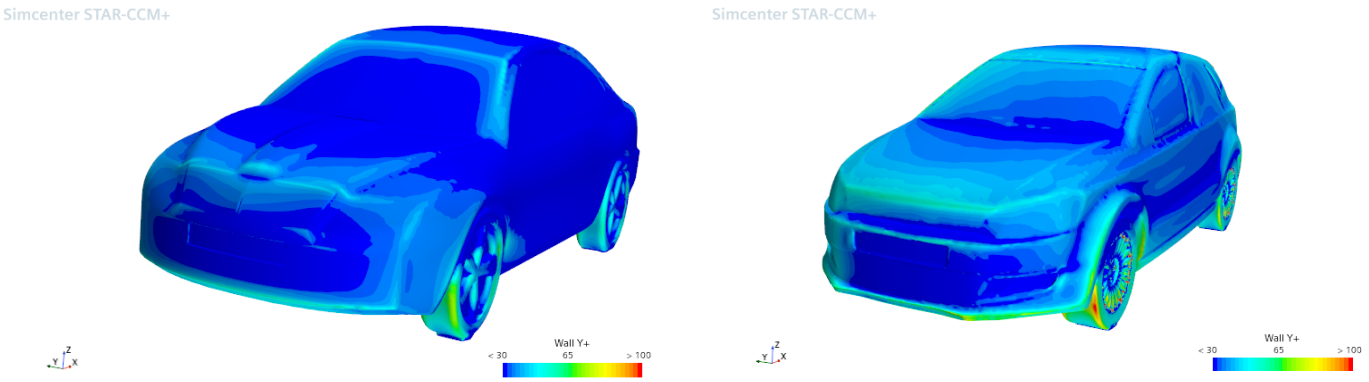


(a) Notchback (b) Hatchback

**Figure 8.** Wall-$y^+$ distribution for both vehicle configurations at mesh level M4: (a) Notchback; (b) Hatchback.

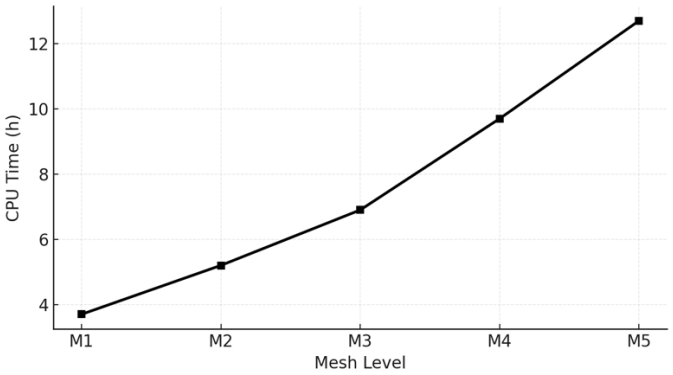


(a)

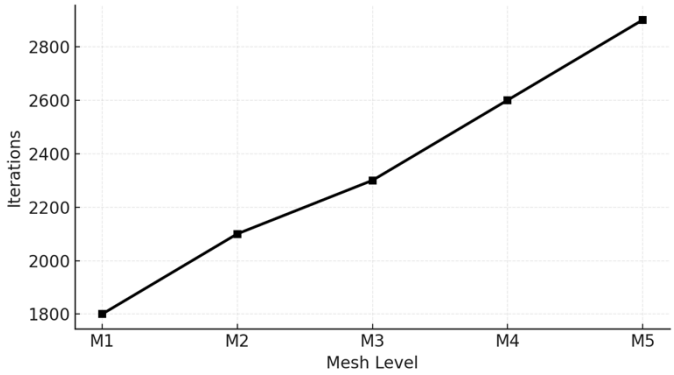


(b)

**Figure 9.** Computational cost versus mesh level M1–M5: (a) CPU time per simulation; (b) number of iterations to convergence.

**Table 3.** Computational Cost and Convergence Metrics for Mesh Levels M1–M5.

| Mesh Level | CPU Time (h) | Iterations |
|---|---|---|
| M1 | 3.7 | 1800 |
| M2 | 5.2 | 2100 |
| M3 | 6.9 | 2300 |
| M4 | 9.7 | 2600 |
| M5 | 12.7 | 2900 |

Most importantly, the Prism Layer construction remained cohesive at both vehicles and even exhibited a similar pattern at the more geometrically complex rear hatch curvature of the Hatchback model. The near-wall resolution satisfies the requirements for Wall-Modeling in the SST k-ω Framework. For both Geometries, approximately 95% of the wall-adjacent cells reside in the Target Placement Range for logarithmic-layer placement, ensuring that turbulence production is Physically Consistent and that the wall-shear evaluation is stable. The concentration of high y+ values around the wheels is a well-documented, albeit generally a little more acute, artefact of rotating-wheel aerodynamics, even when wheels are modeled as Stationary Solids, and is within acceptable limits and does not affect the global convergence behavior.

The mesh-quality indicators indicated that M4 is smooth, orthogonal, and near-wall compliant and therefore satisfied the Monotonic Cd Convergence Trend and the Reynolds-number stabilization behavior described in Sections 4.1 and 4.2, respectively. The absence of Oscillations in the Force-History data and the instantaneous convergence of Drag among both Models further support the conclusion that the Mesh does not impose numerical artefacts which mask or distort the physical flow characteristics.

### 4.4. Computational Cost and Convergence Behavior

In order to evaluate the trade-off between accuracy and computational efficiency of steady RANS simulations, this section contains the amount of CPU time and number of iterations needed for each level of mesh, The trends summarized in Table 3 are visualized in Figure 9, which shows that both CPU time and iteration count increase almost linearly with mesh refinement from M1 to M5.This behavior indicates that the increase in computational cost is mainly driven by the larger cell count, while the solver performance is not adversely affected by mesh stiffness. CPU time is directly related to the number of cells in each mesh and scales approximately linearly, demonstrating that the solver was not impacted by stiffness or high levels of mesh non-orthogonality. All simulations were performed on a dual-processor Linux High-Performance Computing (HPC) Workstation with two Intel Xeon processors and 32 parallel compute cores.

This configuration was used due to its high level of parallel efficiency and low amount of inter-processor communication overhead when using more than ~32-48 processors in polyhedral RANS simulations. The HPC workstation used had 128 GB of RAM and employed the MPI-based parallel framework provided with S Simcenter STAR-CCM+, which enabled the consistent level of scaling of the CPU time to the mesh levels from M1 to M5. The residuals decreased by $10^{-3}$ from the first to the last mesh across all simulation runs, while the force histories of each run converged smoothly without oscillations (the convergence characteristics were discussed in Section 4.3).

The difference in the drag coefficients for mesh levels M4 and M5 remained below 1.5% for both geometries (≈1.4% for the Notchback and ≈1.2% for the Hatchback), which is consistent with common mesh-independence criteria established for automotive aerodynamics. Thus, the performance of mesh level M4 is the best compromise, as it provides nearly identical drag coefficients as mesh level M5 but is more efficient and reduces costs by greater than 20% compared to M5. This trend of M4 out-performing M5 applies to both aerodynamic geometries, Notchback and Hatchback, indicating that the refinement strategy provides generalizes robustly across disparate rear-end designs.

### 4.5. Mesh Strategy and Flow-Modeling Implications

Observations made at levels of refinement M1–M5 illustrate that the prediction of drag for both the Notchback and Hatchback at level M4 is not dependent upon the actual number of cells in the grid, but rather how resolution is distributed around the important flow features associated with each vehicle. Once the A-pillar vortices, roof-rear separation line, and shear layers in the near-wake region were adequately resolved, improvements to the predicted drag (i.e., convergence of the mesh) for either vehicle became unaffected by any further refinement of the grid. The conclusion that the underlying flow physics govern point of convergence, rather than simply the mesh density, is supported by the activity of the SST k-ω model which produced stable results when skewness of polyhedral cells was controlled and consistent $y^+$ band thus, ultimately leading to the successful capture of the primary modes of separation under the fixed 15° yaw condition for both models. The insights gained from the approach described in the foregoing will allow for improved accuracy–cost efficiency with respect to refinement targeted toward separation-driven structures. This refinement strategy may also serve as a guide for performing steady-RANS simulations of future passenger vehicle designs with similar aerodynamic characteristics.

## 5. Limitations and Future Work

This study has some inherent limitations. All simulations are based on steady incompressible RANS with the SST k–ω model, and thus unsteady wake dynamics and transient crosswind effects are not resolved and only time-averaged loads are assessed. The vehicle geometries are simplified, with small-scale details omitted (e.g., mirrors/wipers) and the wheels modelled as stationary rather than rotating and the analysis is restricted to two rear-end typologies at a single yaw angle of 15° over a limited full scale Re range. Moreover, the focus is on numerical verification rather than full experimental validation because no dedicated wind-tunnel or on-road data are available for direct comparison. Future work should thus integrate the current verification framework with detailed experimental measurements of similar vehicle configurations with crosswind. Hybrid RANS–LES or other scale resolving approaches could be applied on more refined versions of this verified mesh to study unsteady loads, rotating wheels and a more detailed underbody. An interesting extension would be to test the proposed refinement strategy under more complex and realistic operating conditions such as additional body styles, multiple yaw angles and gust-like crosswind events.

## 6. Conclusion

The mesh refinement study conducted on the two vehicles, Notchback and Hatchback indicates that grid level M4 produced a mesh-independent solution for the drag with less than 2% variation with respect to the drag from M5, and reduced computational cost by over 20%.

At a fixed yaw angle (15°), both designs exhibit similar trends with Re with both Cd values approaching an asymptotic value at a Re of approximately $1.5\times10^7$ indicating the transition from a fully turbulent boundary layer and the geometry-dependent wake structure. Therefore, refining mesh resolution for targeted areas such as separation areas, curvature changes and near-wake region instead of implementing uniform refinement throughout the entire mesh is a more efficient method of completing full-scale automotive RANS simulations at steady, high Re conditions.

Results of this project can be used to complete steady-state, high-Re flows for vehicle geometries of similar shapes. Future work may include expanding this analysis on the effects of transient aerodynamic loads resulting from wind disturbances, the inclusion of the effects of vehicle wheels while in motion, the combination of using RANS and LES in a hybrid RANS-LES methodology.

## 7. Declarations

### 7.1. Author Contributions

**Mohammed ALmaghrebi:** Conceptualization, Methodology, Software, Validation, Formal analysis, Investigation, Resources, Data curation, Writing – original draft, Writing – review & editing, Visualization, Supervision, Project administration; **Ahmed Atta Elhussein Ali:** Writing – review & editing.

### 7.2. Institutional Review Board Statement

Not applicable. This study did not involve human participants, animals or clinical data.

### 7.3. Informed Consent Statement

Not applicable. No human subjects were involved in this research.

### 7.4. Data Availability Statement

The data that support the findings of this study, including the CAD geometries, mesh templates and post-processed aerodynamic coefficients, are available from the corresponding author upon reasonable request.

### 7.5. Acknowledgment

The authors gratefully acknowledge the support and facilities provided by the Faculty of Engineering, Al-Saeeda University, Yemen, the School of Automotive Engineering, Wuhan University of Technology, 430070, China, and the School of Business, Sichuan University, China.

### 7.6. Conflicts of Interest

The authors declare no conflicts of interest.

## 8. References

[1] J. H. Ferziger, M. Perić, and R. L. Street, *Computational Methods for Fluid Dynamics*. Springer, 2019. https://doi.org/10.1007/978-3-319-99693-6.

[2] S. B. Pope, *Turbulent Flows*. Cambridge Univ. Press, 2000. https://doi.org/10.1016/S0010-2180(01)00244-9.

[3] T. Cebeci, *Analysis of Turbulent Flows: With Computer Programs*. Springer, 2009. https://books.google.co.id/books?id=UX_hXE4luVMC.

[4] M. A. A. Al-Maghrebi *et al.*, "Aerodynamic design and performance evolution of notchback vehicles," *Eur. J. Appl. Sci., Eng. Technol.*, vol. 3, no. 5, pp. 78–87, 2025, https://doi.org/10.59324/ejaset.2025.3(5).06.

[5] J. Hüttenrauch, "The second generation of the VW Polo BlueMotion," *ATZ Worldw.*, vol. 112, pp. 16–23, Feb. 2010, https://doi.org/10.1007/BF03225112.

[6] C. Repmann and M. Hähnel, "The aerodynamics development of the new Volkswagen Polo," in *Progress in Vehicle Aerodynamics and Thermal Management (FKFS 2017)*, J. Wiedemann, Ed. Cham, Switzerland: Springer, 2018, pp. 160–167, https://doi.org/10.1007/978-3-319-67822-1_10.

[7] A. Kazi, P. Acharya, A. Patil, and A. Noraje, "Effect of spoiler design on hatchback car," *Int. J. Mod. Trends Eng. Res.*, vol. 3, no. 9, pp. 192–200, 2016. https://scispace.com/pdf/effect-of-spoiler-design-on-hatchback-car-539a43rt0h.pdf.

[8] O. Čavoj, O. Blaťák, P. Hejtmánek, and J. Vančura, "Vehicle ride height change due to radial expansion of tires," *Mach. Dyn. Diagn.*, 2015, https://doi.org/10.1515/mecdc-2015-0008.

[9] B. N. Zakher, M. Elhadary, M. A. El-Gohary, and I. M. El Fahham, "Comparison between experimental life road simulation and computational fluid dynamics and fluid structure interaction for sedan car," *CFD Lett.*, vol. 14, no. 2, pp. 81–97, 2022, https://doi.org/10.37934/cfdl.14.2.8197.

[10] L. Jiang, H. Liu, G. Chai, G. Jiang, and W. Lin, "Effect of automotive headlamp modeling on automotive aerodynamic drag," in *Proc. 2008 9th Int. Conf. Computer-Aided Industrial Design and Conceptual Design (CAIDCD)*, Kunming, China, Nov. 2008, pp. 588–593, https://doi.org/10.1109/CAIDCD.2008.4730637.

[11] F. R. Menter, "Two-equation eddy-viscosity turbulence models for engineering applications," *AIAA J.*, vol. 32, no. 8, pp. 1598–1605, 1994. https://doi.org/10.2514/3.12149.

[12] P. J. Roache, *Verification and Validation in Computational Science and Engineering*. Hermosa Publishers, 1998. https://lccn.loc.gov/98096214.

[13] B. C. Ismail *et al*, "Procedure for estimation and reporting of uncertainty due to discretization in CFD applications," *J. Fluids Eng.*, vol. 130, no. 7, p. 078001, 2008. https://doi.org/10.1115/1.2960953.

[14] A. N. N. Azman, K. Venkatason, and S. Sivaguru, "Mesh convergence analysis on the aerodynamic performance of a sedan vehicle," *J. Eng. Technol. Appl. Phys.*, vol. 7, no. 1, pp. 85–95, 2025. https://doi.org/10.33093/jetap.2025.7.1.14.

[15] A. Ghavidel, M. Rashki, H. G. Arab, and M. A. Moghaddam, "Reliability mesh convergence analysis by introducing expanded control variates," *Front. Struct. Civ. Eng.*, vol. 14, no. 4, pp. 1012–1023, 2020. https://doi.org/10.1007/s11709-020-0631-6.

[16] N. Ashton, P. Unterlechner, and T. Blacha, "Assessing the sensitivity of hybrid RANS-LES simulations to mesh resolution, numerical schemes and turbulence modelling within an industrial CFD process," *SAE Tech. Paper* 2018-01-0709, 2018. https://doi.org/10.4271/2018-01-0709.

[17] C. Zhang, C. P. Bounds, L. Foster, and M. Uddin, "Turbulence modeling effects on the CFD predictions of flow over a detailed full-scale sedan vehicle," *Fluids*, vol. 4, no. 3, p. 148, 2019. https://doi.org/10.3390/fluids4030148.

[18] E. Guilmineau, "Numerical simulations of flow around a realistic generic car model," *SAE Int. J. Passeng. Cars–Mech. Syst.*, vol. 7, pp. 646–653, 2014. https://doi.org/10.4271/2014-01-0607.

[19] M. N. F. Kamal *et al.*, "A review of aerodynamics influence on various car model geometry through CFD techniques," *J. Adv. Res. Fluid Mech. Therm. Sci.*, vol. 88, no. 1, pp. 109–125, 2021. https://doi.org/10.37934/arfmts.88.1.109125.

[20] M. G. Connolly, A. Ivankovic, and M. J. O'Rourke, "Drag reduction technology and devices for road vehicles – a comprehensive review," *Heliyon*, vol. 10, no. 13, p. e33757, 2024. https://doi.org/10.1016/j.heliyon.2024.e33757.

[21] S. Sarkar, K. Thummar, N. Shah, and V. Vagrecha, "A review paper on aerodynamic drag reduction and CFD analysis of vehicles," *Proc. A Rev. Paper Aerodyn. Drag Reduct. CFD Anal. Vehicles*, pp. 231–235, 2019. https://doi.org/10.13140/RG.2.2.31506.91849.

[22] R. F. Soares, "Drag of road cars: cost-effective CFD setup, proposal of an aerodynamic concept and case studies," 2015. https://doi.org/10.14393/ufu.di.2015.352.

[23] C. W. Hirt and B. D. Nichols, "Volume of fluid (VOF) method for the dynamics of free boundaries," *J. Comput. Phys.*, vol. 39, no. 1, pp. 201–225, 1981. https://doi.org/10.1016/0021-9991(81)90145-5.

[24] M. Schlipf, A. Tismer, and S. Riedelbauch, "On the application of hybrid meshes in hydraulic machinery CFD simulations," *IOP Conf. Ser.: Earth Environ. Sci.*, vol. 49, p. 062013, 2016. https://doi.org/10.1088/1755-1315/49/6/062013.

[25] V. Kausalyah *et al.*, "Optimisation of vehicle front-end geometry for adult and pediatric pedestrian protection," *Int. J. Crashworthiness*, vol. 19, no. 2, pp. 153–160, 2014. https://doi.org/10.1080/13588265.2013.879506.

[26] M. Braza, P. Chassaing, and H. H. Minh, "Numerical study and physical analysis of the pressure and velocity fields in the near wake of a circular cylinder," *J. Fluid Mech.*, vol. 165, pp. 79–130, 1986. https://doi.org/10.1017/S0022112086003014.

[27] Y. Wang, C. Wu, G. Tan, and Y. Deng, "Reduction in the aerodynamic drag around a generic vehicle by using a non-smooth surface," *J. Automob. Eng.*, vol. 231, no. 1, pp. 130–144, 2017. https://doi.org/10.1177/0954407016636970.

[28] M. N. Sudin, M.A. Abdullah, S. A. Shamsuddin, F. R. Ramli, and M. M. Tahir, "Review of research on aerodynamic drag reduction methods," *Int. J. Mech. Mechatronics Eng. (IJMME-IJENS)*, vol. 14, no. 2, 2014. https://eprints.utem.edu.my/id/eprint/12204/1/145302-6868-IJMME-IJENS.pdf.

[29] K. Nisugi, T. Hayase, and A. Shirai, "Fundamental study of aerodynamic reduction for vehicle with feedback flow control," *JSME Int. J., Ser. B*, vol. 47, no. 3, 2004. https://doi.org/10.1299/jsmeb.47.584.

[30] F. Mariani, C. Pogianni, F. Risi, and L. Scappaticci, "Formula SAE racing car: Experimental and numerical analysis of the external aerodynamics," in *69th Conf. Italian Thermal Machines Eng. Assoc. (ATI 2014)*, 2014. https://doi.org/10.1016/j.egypro.2015.12.111.

[31] A. Javed, K. Djijdeli, and J. T. Xing, "A coupled meshfree-mesh-based solution scheme on hybrid grid for flow-induced vibrations," *Acta Mech.*, vol. 227, no. 8, pp. 2245–2274, 2016. https://doi.org/10.1007/s00707-016-1614-5.

[32] N. R. Morgan and J. I. Waltz, "3D level set methods for evolving fronts on tetrahedral meshes with adaptive mesh refinement," *J. Comput. Phys.*, vol. 336, pp. 492–512, 2017. https://doi.org/10.1016/j.jcp.2017.02.030.

[33] M. Alam, K. Walters, and D. Thompson, "A transition-sensitive hybrid RANS/LES modeling methodology for CFD applications," in *51st AIAA Aerospace Sciences Meeting including the New Horizons Forum and Aerospace Exposition*, Grapevine, TX, USA, 2013, p. 995. https://doi.org/10.2514/6.2013-995.

[34] S. Jakirlic, L. Kutej, B. Basara, and C. Tropea, "Computational study of the aerodynamics of a realistic car model by means of RANS and hybrid RANS/LES approaches," *SAE Int. J. Passeng. Cars – Mech. Syst.*, vol. 7, no. 2, pp. 559–574, 2014. https://doi.org/10.4271/2014-01-0594.